Inorganic Chemistry
Article
pubs.acs.org/IC

Revelation of Varying Bonding Motif of Alloxazine, a Flavin Analogue, in Selected Ruthenium(II/III) Frameworks

Prasenjit Mondal, Ritwika Ray, Ankita Das, and Goutam Kumar Lahiri*

Department of Chemistry, Indian Institute of Technology Bombay, Powai, Mumbai, India 400076

Ⓢ *Supporting Information*

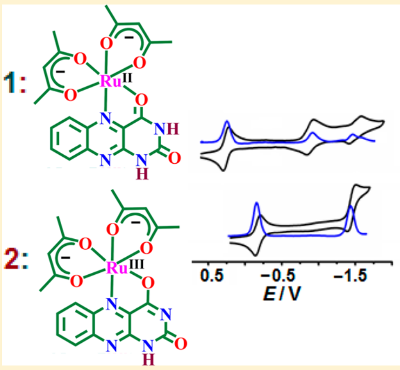

ABSTRACT: The reaction of alloxazine (L) and $Ru^{II}(acac)_2(CH_3CN)_2$ ($acac^-$ = acetylacetonate) in refluxing methanol leads to the simultaneous formation of $Ru^{II}(acac)_2(L)$ (**1** = bluish-green) and $Ru^{III}(acac)_2(L^-)$ (**2** = red) encompassing a usual neutral α-iminoketo chelating form of L and an unprecedented monodeprotonated α-iminoenolato chelating form of L^-, respectively. The crystal structure of **2** establishes that N5,O4$^-$ donors of L^- result in a nearly planar five-membered chelate with the $\{Ru^{III}(acac)_2{}^+\}$ metal fragment. The packing diagram of **2** further reveals its hydrogen-bonded dimeric form as well as π−π interactions between the nearly planar tricyclic rings of coordinated alloxazine ligands in nearby molecules. The paramagnetic **2** and one-electron-oxidized $\mathbf{1}^+$ display ruthenium(III)-based anisotropic axial EPR in CH_3CN at 77 K with $\langle g\rangle/\Delta g$ of 2.136/0.488 and 2.084/0.364, respectively ($\langle g\rangle = \{1/3(g_1{}^2 + g_2{}^2 + g_3{}^2)\}^{1/2}$ and $\Delta g = g_1 - g_3$). The multiple electron-transfer processes of **1** and **2** in CH_3CN have been analyzed by DFT-calculated MO compositions and Mulliken spin density distributions at the paramagnetic states, which suggest successive two-electron uptake by the π-system of the heterocyclic ring of L ($L \rightarrow L^{\bullet-} \rightarrow L^{2-}$) or L^- ($L^- \rightarrow L^{\bullet 2-} \rightarrow L^{3-}$) besides metal-based ($Ru^{II}/Ru^{III}$) redox process. The origin of the ligand as well as mixed metal−ligand-based multiple electronic transitions of $\mathbf{1}^n$ (n = +1, 0, −1, −2) and $\mathbf{2}^n$ (n = 0, −1, −2) in the UV and visible regions, respectively, has been assessed by TD-DFT calculations in each redox state. The pK_a values of **1** and **2** incorporating two and one NH protons of 6.5 (N3H, pK_{a1})/8.16 (N1H, pK_{a2}) and 8.43 (N1H, pK_{a1}), respectively, are estimated by monitoring their spectral changes as a function of pH in CH_3CN-H_2O (1:1). **1** and **2** in CH_3CN also participate in proton-driven internal reorganizations involving the coordinated alloxazine moiety, i.e., transformation of an α-iminoketo chelating form to an α-iminoenolato chelating form and the reverse process without any electron-transfer step: $Ru^{II}(acac)_2(L)$ (**1**) → $Ru^{II}(acac)_2(L^-)$ ($\mathbf{2}^-$) and $Ru^{III}(acac)_2(L^-)$ (**2**) → $Ru^{III}(acac)_2(L)$ ($\mathbf{1}^+$).

■ INTRODUCTION

The redox-active heterocyclic isoalloxazine moiety of flavin in flavoenzymes participates in successive two-electron reductions to yield flavohydroquinone via the formation of intermediate flavosemoquinone (Scheme 1).[1] Although the metal ions in the vicinity of flavoenzymes facilitate the intraprotein electron-transfer processes,[2] the coordination of flavin with the metal ions in the enzymes has yet not been recognized.[3] This indeed has spurred the development of model metal complex frameworks of flavin and its tricyclic analogue alloxazine or isoalloxazine (Scheme 2) in order to understand (i) their coordinating mode(s), (ii) metal ion prompted electron-transfer processes including the effect of noncovalent interactions (hydrogen bonding and π−π interaction), and (iii) accessibility of the intermediate radical state.[4,3b]

Earlier studies have established selective coordination of neutral N5,O4 donors of flavin and its tricyclic analogue alloxazine or isoalloxazine (Scheme 2) to the metal ions, resulting in a planar five-membered α-iminoketo chelate ring.[3b,5] The unusual N1$^-$,N10-donating four-membered chelating mode of monodeprotonated alloxazine has, however, been reported recently in a structurally characterized mononuclear $[Ru^{II}(Hallo)(tpa)]PF_6$ (**4**) (Scheme 3) complex (H_2allo = alloxazine; tpa = tris(2-pyridylmethyl)amine).[6] This has introduced the additional impetus of probing the effect of hitherto unexplored metal fragments with the broader perspectives of extending further insights into the mode of metal−alloxazine interaction and the subsequent electron-transfer aspects.

In this regard, the present Article demonstrates the remarkable impact of the selective metal fragment $\{Ru(acac)_2\}$ incorporating electron-rich $acac^-$ (acetylacetonate) in stabilizing the unprecedented coordinating mode of alloxazine in the discrete molecular framework of **2** (Scheme 3), involving a ruthenium(III)-bonded α-iminoenolato (−N5═C−C(−O4$^-$)−) chelate ring, along with the ruthenium(II)-bonded usual α-iminoketo (−N5═C−C(═O4)−) chelate ring in **1** (Scheme 3). The N5,O4-bonded α-iminoketo chelating form of 1,3-dimethylalloxazine has also been reported in combination with the analogous metal unit $\{Ru(bpy)_2\}^{2+}$ (**3**) involving the π-acidic bpy (bpy = 2,2′-bipyridine) ligand (Scheme 3).[7]

Received: January 19, 2015
Published: March 4, 2015

DOI: 10.1021/acs.inorgchem.5b00122
Inorg. Chem. 2015, 54, 3012−3021

Scheme 1. Electron-Transfer Processes of Flavin

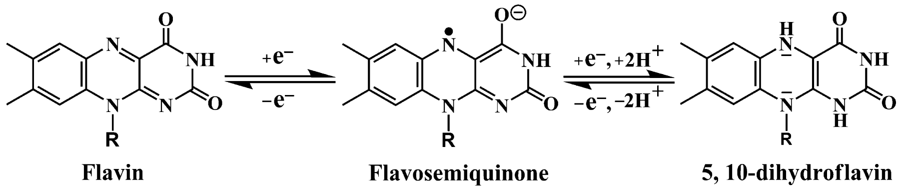

Scheme 2. Structural Forms of Alloxazine and Isoalloxazine

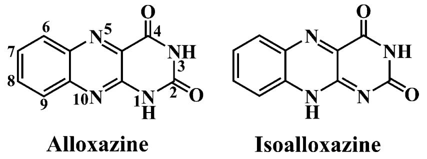

Herein, we report the synthetic account of **1** and **2** including the structural characterization of **2** and electronic structural aspects in accessible redox states of $\mathbf{1}^n$ (n = +1, 0, −1, −2) and $\mathbf{2}^n$ (n = 0, −1, −2) by experimental investigations (electrochemistry, spectroelectrochemistry, EPR) in conjunction with DFT/TD-DFT calculations and proton-driven internal reorganization processes.

RESULTS AND DISCUSSION

Synthesis, Structure, and Spectroscopic Characterization. The reaction of the metal precursor $Ru^{II}(acac)_2(CH_3CN)_2$ ($acac^-$ = acetylacetonate) and the commercially available alloxazine (L) in refluxing methanol under aerobic condition followed by chromatographic separation on a silica gel column using CH_2Cl_2−CH_3CN (1:1) and CH_3CN−MeOH (30:1) as eluants results in complexes **1** (bluish-green) and **2** (red), respectively, in 2:1 ratio. Different analytical (microanalysis, molar conductivity, mass, IR, NMR, EPR, UV−vis) studies including the crystal structure analysis of **2** (see later) establish the identities of the complexes. The alloxazine ligand (L) (Scheme 4) binds to the ruthenium(II) ion through the neutral N5,O4 donors (amide form) in $Ru^{II}(acac)_2(L)$ (**1**), as has been reported in most of the other metal complexes of L,[3b,5,7,8] while the unprecedented monodeprotonated imidate form of alloxazine (L^-) (Scheme 4) links to the ruthenium(III) ion via the monoanionic N5,$O4^-$ donors in $Ru^{III}(acac)_2(L^-)$ (**2**). The presence of three anionic ligands (two $acac^-$ and L^-) around the metal ion indeed facilitates the oxidation of the metal ion to the ruthenium(III) state in **2** under an aerobic reaction environment,[9] which has also been nicely reflected in their redox potentials (see later).

Complex **2** is found to be perfectly stable in both the solid and solution states. The partial slow transformation of **1** to **2** however takes place over a period of days presumably via the emancipation of H_2 (Scheme 4), which indeed has restricted us in generating the crystals of **1** for its structural characterization.

Scheme 4. Slow Transformation of 1 → 2

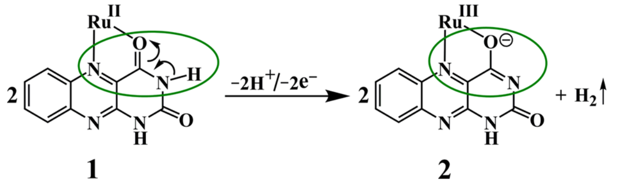

The electrically neutral complexes give satisfactory microanalytical data (Experimental Section). ESI(+) mass spectrometry shows molecular ion peaks (m/z) at 514.0449 and 513.2674, corresponding to **1** (calculated mass: 514.0420) and **2** (calculated mass: 513.0348), respectively (Experimental Section and Figure S1, Supporting Information). Complex **1** is diamagnetic (Ru^{II}, S = 0), and one-electron paramagnetic **2** (Ru^{III}, S = 1/2) exhibits a magnetic moment, $\mu_{eff.}$ =1.88 μ_B, in the solid state at 298 K.[10]

The imidate form of the monodeprotonated L^- in **2** has been authenticated by its single-crystal X-ray structure (Figure 1).

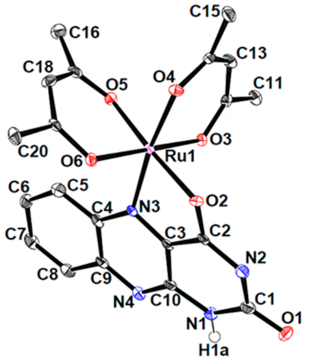

Figure 1. ORTEP diagram of **2**. Ellipsoids are drawn at the 50% probability level. Hydrogen atoms (except the NH proton) are omitted for clarity.

Scheme 3. Representation of Complexes 1−4

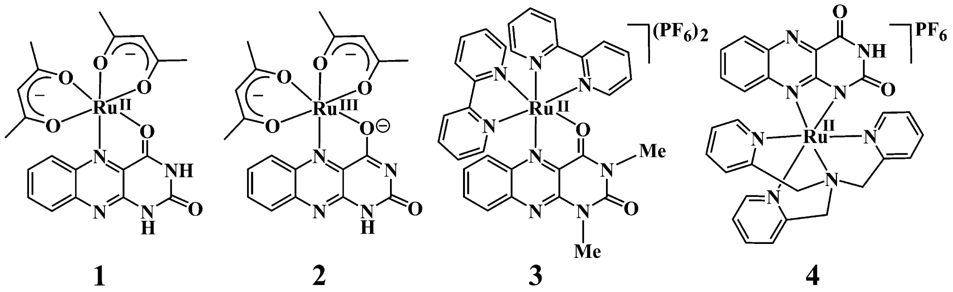

The selected crystallographic parameters and bond parameters are set in Tables 1, 2, S1, and S2 (Supporting Information), respectively. The monodeprotonated alloxazine ligand (L^-) binds to the ruthenium ion in **2** through its N5,O4$^-$ donors, leading to a five-membered bidentate chelate. The monoanionic α-iminoenolato chelate ring (imidate motif, Scheme 4) in **2** instead of the α-iminoketo chelate ring (amide motif, Scheme 4) has been evident by the relevant C2−N2, C2−O2, C2−C3, C3−C10, N3−C3, and N3−C4 bond distances of 1.319(5), 1.291(4), 1.459(5), 1.414(5) , 1.333(5), and 1.376(5) Å, respectively. The imidate form of the pterin ligand has also been reported in ruthenium(II) complexes, $[Ru^{II}(dmdmp)(TPA)]ClO_4$ and $[Ru^{II}(dmp)(TPA)]ClO_4$ (Hdmdmp = 3-(*N*,*N*-dimethyl)-6,7-dimethylpterin, Hdmp = 6,7-dimethylpterin, TPA = tris(2-pyridylmethyl)amine).[11] The only other reported crystal structure of the ruthenium-coordinated alloxazine in $[Ru^{II}(Hallo)(tpa)]PF_6$ (**4**) (Scheme 3) reveals its unusual monodeprotonated N1$^-$,N10 coordinating mode, resulting in a four-membered chelate.[6a] The neutral N5,O4 (i.e., amide form) binding mode of 1,3-dimethylalloxazine (DMA), 1,3,7,8-tetramethylalloxazine (tmazH), and alloxazine has been reported in $(DMA)WO_2Cl_2$[7]/$[(DMA)IrCp^*Cl]PF_6$,[5f] $Mo(O)Cl_3(tmazH)$,[12] and $[Ir_4(Allo)(Cp^*)_4(Hallo)_2Cl_2](PF_6)_2$, respectively.[13] *To the best of our knowledge, complex* **2** *represents the first structurally characterized metal-coordinated N5,O4*$^-$*-donating imidate form of the monodeprotonated alloxazine ligand (*L^-*).*

Table 1. Selected Crystallographic Data for 2

empirical formula	$C_{20}H_{19}N_4O_6Ru$
fw	512.46
cryst syst	triclinic
space group	$P\bar{1}$
a (Å)	7.506(3)
b (Å)	10.903(4)
c (Å)	13.563(5)
α (deg)	68.519(13)
β (deg)	76.490(17)
γ (deg)	75.877(16)
V (Å^3)	988.8(6)
Z	2
μ (mm^{-1})	0.840
T (K)	100
D_{calcd} (g cm^{-3})	1.721
F(000)	518
θ range (deg)	3.04 to 25.00
data/restraints/params	3462/0/280
R_1, wR_2 [$I > 2\sigma(I)$]	0.0427, 0.0864
R_1, wR_2 (all data)	0.0485, 0.0899
GOF	1.078
largest diff peak/hole (e Å^{-3})	0.606/−0.838

Table 2. Experimental and DFT-Calculated Selected Bond Lengths for 2

bond length	X-ray (Å)	DFT (Å)
Ru1−O2	2.045(3)	2.024
Ru1−O3	2.008(3)	2.023
Ru1−O4	2.017(3)	2.046
Ru1−O5	1.992(3)	2.060
Ru1−O6	1.998(3)	2.046
Ru1−N3	2.060(3)	2.138
O1−C1	1.227(5)	1.217
O2−C2	1.291(4)	1.299
N1−C1	1.399(5)	1.428
N1−C10	1.375(5)	1.361
N2−C1	1.390(5)	1.384
N2−C2	1.319(5)	1.306
N3−C3	1.333(5)	1.325
N3−C4	1.376(5)	1.373
C3−C2	1.459(5)	1.472
C3−C10	1.414(5)	1.424

The heteroatomic tricyclic ring of L^- as well as the five-membered chelate in **2** are nearly planar. The bite angles involving L^- (N3−Ru1−O2, 80.51(11)°) and acac$^-$ (O3−Ru1−O4, 93.20(11)°, O5−Ru1−O6, 91.34(11)°) ligands and the *trans* angles O3−Ru1−O6, 177.15(10)°, O4−Ru1−N3, 171.96(12)°, and O5−Ru1−O2, 175.47(11)° in **2** collectively suggest a distorted octahedral geometry around the ruthenium ion. The Ru^{III}−O2 and Ru^{III}−N3 bond distances are 2.045(3) and 2.060(3) Å, respectively. The average Ru^{III}−O(acac$^-$) bond distance of 2.004(3) Å in **2** matches well with the reported analogous $\{Ru^{III}(acac)_2\}$ complexes.[14] The C1−O1 bond distance of coordinated L^-, 1.227(5) Å, is attributesd to the free carbonyl function.[15] The bond parameters of **2** have been well reproduced by the corresponding DFT-optimized structure (Figure S3, Tables S1, S2, Supporting Information).

Interestingly, the packing diagram of **2** reveals the intermolecular double N1−H1A−O1#1 hydrogen-bonding interactions between the two molecules in the neighboring units, leading to a dimeric form with an N1---O1#1 distance of 2.885(4) Å and N1−H1A−O1#1 angle of 157.5° (#1 = $-x+1$, $-y+2$, $-z+1$) (Figure 2).[16] Further, $\pi-\pi$ interactions take place between the nearly planar tricyclic rings of L^- of two molecules of **2** in the asymmetric unit (3.378 Å) and in the adjacent units (3.429 Å) (Figure 3).[16]

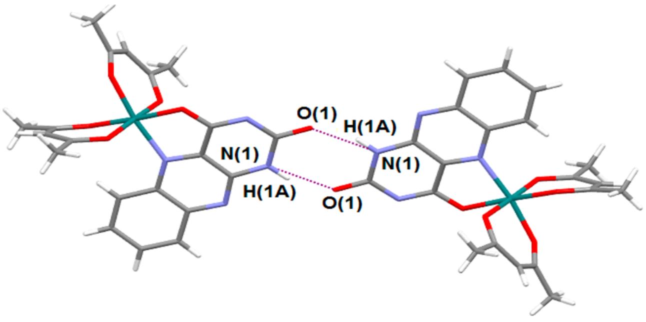

Figure 2. Perspective view showing the intermolecular hydrogen-bonded dimeric form in the crystal of **2**.

Though we failed to generate a suitable single crystal of **1**, particularly due to its partial conversion to **2** during the course of the crystallization process over a period of 10 days or more (Scheme 4), the amide form of the alloxazine ligand (L) in **1** has been corroborated by the DFT-calculated pertinent bond lengths, C2−O2, 1.248 Å; C2−N2, 1.376 Å; C2−C3, 1.440 Å; C3−N3, 1.353 Å; C4−N3, 1.382 Å, and C3−C10, 1.413 Å (Figure S2, Tables S3, S4, Supporting Information), which match fairly well with those of the earlier reported analogous complexes $(DMA)WO_2Cl_2$,[7] $[(DMA)IrCp^*Cl]PF_6$,[5f] and $Mo(O)Cl_3(tmazH)$.[12]

The IR spectra (KBr disc) of **1** and **2** display strong vibrations at 1713 and 1667 cm^{-1}, corresponding to the free

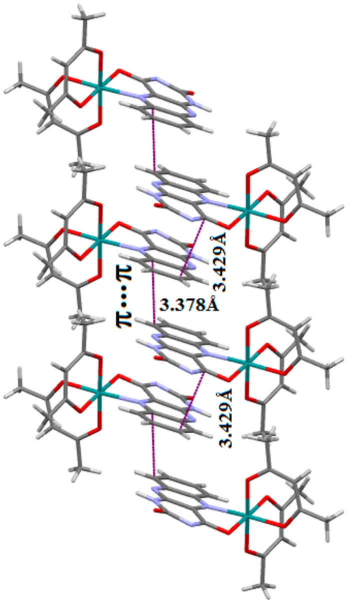

Figure 3. π−π interactions between the nearly planar tricyclic rings of two molecules of **2**.

carbonyl function (ν(C═O)) of ruthenium(II)-coordinated L[17] and ruthenium(III)-coordinated L^-, respectively.

The ^1H NMR spectrum of diamagnetic **1** in CD_3CN (Figure 4, Experimental Section) exhibits well-defined aromatic (L) and aliphatic (acac) proton resonances at δ 8.03−7.52 ppm and 5.68−1.95 ppm, respectively. The D_2O-exchangeable two NH proton resonances appear as an overlapping broad peak centered at δ 9.60 ppm. The paramagnetic complex **2** exhibits broad proton resonances of L^- and $acac^-$ over a wide chemical shift range of δ 7 to −23 ppm in $CDCl_3$ due to a paramagnetic contact shift effect[18] (Figure 4, Experimental Section). The D_2O-exchangeable NH proton of **2** appears at a much higher chemical shift of δ 4.95 ppm.

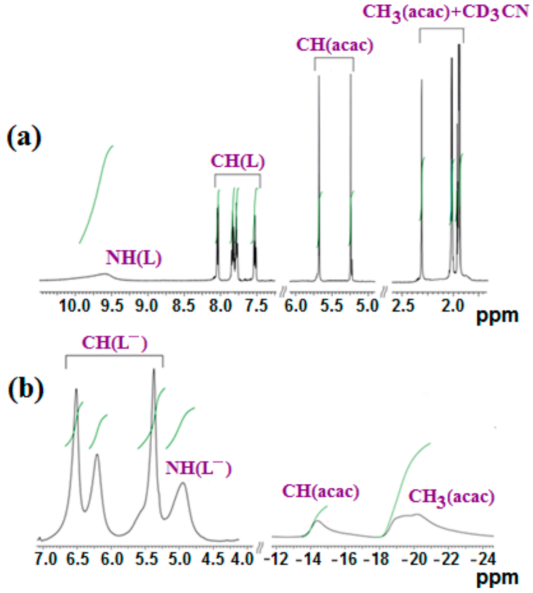

Figure 4. ^1H NMR spectra of (a) **1** in CD_3CN and (b) **2** in $CDCl_3$.

Electrochemistry, EPR, and DFT Calculations. The redox potentials of **1** and **2** including the other known ruthenium-alloxazine complexes (**3** and **4**) are listed in Table 3. Complex **1** displays one reversible oxidation (Ox1), E^0, V (ΔE_p, V) at 0.26 (0.08) and two stepwise quasi-reversible reductions, E^0, V (ΔE_p, V) at −0.89 (0.08) (Red1) and −1.50 (0.16) (Red2) in CH_3CN, while **2** exhibits successive two reductions E^0, V (ΔE_p, V) at −0.17 (0.07) (Red1) and −1.44 (0.10) (Red2) (Figure 5, Table 3). The redox processes associated with **1** and **2** have been interpreted via the DFT-calculated MO compositions (Table 4 and Tables S5−S11, Supporting Information) and by Mulliken spin-density distributions at the paramagnetic states (Figure 6, Table 5). The $\{Ru(acac)_2\}$-dominated HOMO (S = 0, 94%) of **1** and β-LUMO (S = 1/2, 84%) of $\mathbf{1}^+$ as well as metal-based spin (0.766) in $\mathbf{1}^+$ justify the correspondence of Ox1 to the Ru^{II}/Ru^{III} process. The alloxazine (L)-dominated LUMO (S = 0, 77%) of **1**, SOMO (S = 1/2, 78%) and β-LUMO (S = 1/2, 81%) of $\mathbf{1}^-$, and HOMO (S = 0, 87%) of $\mathbf{1}^{2-}$ along with L-based spin in $\mathbf{1}^-$ (0.877) suggest the involvement of the coordinated alloxazine in the successive reduction processes L → $L^{\bullet-}$ (Red1) and $L^{\bullet-}$ → L^{2-} (Red2) (Schemes 5, 6).[6a,7,20] The minor metal contribution (18%) in the LUMO of **1** or SOMO of $\mathbf{1}^-$ and in the Mulliken spin distribution in $\mathbf{1}^-$ (Ru: 0.124) is attributed to the weak (dπ)Ru^{II} → (π*)L back-bonding.[10,21] The successive irreversible reductions of free alloxazine occur at −0.87 and −1.44 V in DMF versus SCE,[6a,19] which become more facile and reversible on metalation.

On the other hand, $\{Ru(acac)_2\}$-dominated β-LUMO (S = 1/2, 89%) of the paramagnetic **2** and the HOMO (S = 0, 91%) of $\mathbf{2}^-$ support metal-based first reduction process (Ru^{III}/Ru^{II}, Red1). The involvement of the coordinated L^- in the second reduction process (Red2) has been assessed by the MO compositions of $\mathbf{2}^-$ (LUMO, 87% L^-) and $\mathbf{2}^{2-}$ (SOMO, S = 1/2, 87% L^-) as well as based on the spin accumulation on L (0.956) in $\mathbf{2}^{2-}$. The successive reductions of the π-system of the coordinated alloxazine (L in **1** or L^- in **2**) have been further corroborated by the DFT-calculated lengthening of C−N and C−O and shortening of C−C bond distances pertaining to the chelate ring on moving from n = 0 to −1 to −2 in $\mathbf{1}^n$ or $\mathbf{2}^n$ (Scheme 5, Tables S1−S4, Supporting Information).

The Ru^{III}/Ru^{II} potential of 0.26 V (Ox1) for **1** versus SCE has been appreciably negatively shifted to −0.17 V (Red1) in **2** (Figure 5, Table 3) primarily due to the influence of varying coordination motifs of alloxazine (neutral amide form in **1** versus monoanionic imidate form in **2**), which in effect stabilizes the ruthenium(III) state in **2** under atmospheric conditions. As compared to **1**, the Ru^{II}/Ru^{III} oxidation of the analogous $[Ru^{II}(bpy)_2(DMA)](PF_6)_2$ (**3**) (Scheme 3) encompassing neutral N5,O4-donating DMA (amide motif) takes place at 1.51 V versus SCE (Table 3),[7,19] implying the effect of the π-acceptor bpy coligand toward the further stabilization of the ruthenium(II) state.[22] The Ru^{II}/Ru^{III} oxidation potential of the other known ruthenium-alloxazine complex $[Ru^{II}(Hallo)(tpa)]PF_6$ (**4**) (Scheme 3), incorporating monoanionic $N1^-$,N10-bonded alloxazine, is reported to be 0.80 V versus SCE (Table 3).[6a,19] The first reduction of the ruthenium(II)-coordinated neutral amide form of L (L(**1**) → $L^{\bullet-}$($\mathbf{1}^-$)) takes place at −0.89 V versus SCE (Red1, Figure 5), whereas the same for the ruthenium(II)-coordinated mononegative imidate form of L^- (L^- in $\mathbf{2}^-$ → $L^{\bullet 2-}$ in $\mathbf{2}^{2-}$) has been shifted to more negative potential at −1.44 V (Red2, Figure 5), which might have pushed the expected second reduction ($L^{\bullet 2-}$ in $\mathbf{2}^{2-}$ → L^{3-} in $\mathbf{2}^{3-}$) beyond the experimental potential window of −2 V versus SCE. The successive reductions of the coordinated DMA

DOI: 10.1021/acs.inorgchem.5b00122
Inorg. Chem. 2015, 54, 3012−3021

Table 3. Electrochemical Data[a]

complex	E^0 [V] (ΔE_p [V])[b]			ref
	Ox1	Red1	Red2	
1	0.26 (0.08)	−0.89 (0.08)	−1.50 (0.16)	this work
2		−0.17 (0.07)	−1.44 (0.10)	this work
$[Ru^{II}(bpy)_2(DMA)](PF_6)_2$ (**3**)[c]	1.51	−0.23	−1.11	7
$[Ru^{II}(Hallo)(tpa)]PF_6$ (**4**)[d]	0.80 (0.10)	−0.94 (0.10)	−1.42 (0.15)	6a

[a] From cyclic voltammetry in CH_3CN/0.1 M Et_4NClO_4 at 0.05 V s^{-1}. [b] Potential in V versus SCE; peak potential differences ΔE_p [V] in parentheses. [c] From cyclic voltammetry in THF/0.1 M Bu_4NPF_6 at 0.10 V s^{-1} versus SCE.[19] [d] From cyclic voltammetry in CH_3CN/0.1 M Bu_4NPF_6 at 0.10 V s^{-1} versus SCE.[19]

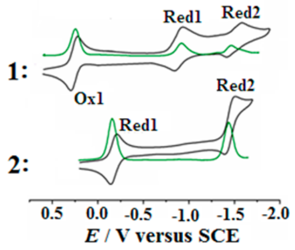

Figure 5. Cyclic (black) and differential pulse (green) voltammograms in CH_3CN.

Table 4. DFT-Calculated Selected MO Compositions for 1^n and 2^n

complex	MO	fragment	% contribution
1 (S = 0)	HOMO	$Ru(acac)_2$	94
	LUMO	Ru/L	18/77
$\mathbf{1}^+$ (S = 1/2)	β-LUMO	$Ru(acac)_2$	84
$\mathbf{1}^-$ (S = 1/2)	SOMO	Ru/L	18/78
	β-LUMO	Ru/L	13/81
$\mathbf{1}^{2-}$ (S = 0)	HOMO	Ru/L	8/87
2 (S = 1/2)	β-LUMO	$Ru(acac)_2$	89
$\mathbf{2}^-$ (S = 0)	HOMO	$Ru(acac)_2$	91
	LUMO	Ru/L^-	11/87
$\mathbf{2}^{2-}$ (S = 1/2)	SOMO	Ru/L^-	10/87

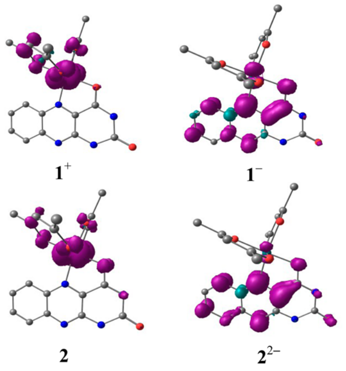

Figure 6. DFT-calculated Mulliken spin density plots of 1^n and 2^n.

Table 5. DFT-Calculated Mulliken Spin Distributions for 1^n and 2^n

complex	Ru	acac	L/L^-
$\mathbf{1}^+$ (S = 1/2)	0.766	0.247	−0.01
$\mathbf{1}^-$ (S = 1/2)	0.124	−0.001	0.877
2 (S = 1/2)	0.818	0.140	0.043
$\mathbf{2}^{2-}$ (S = 1/2)	0.042	0.002	0.956

Scheme 5. Change in DFT-Calculated Bond Distances (Å) on Successive Reductions

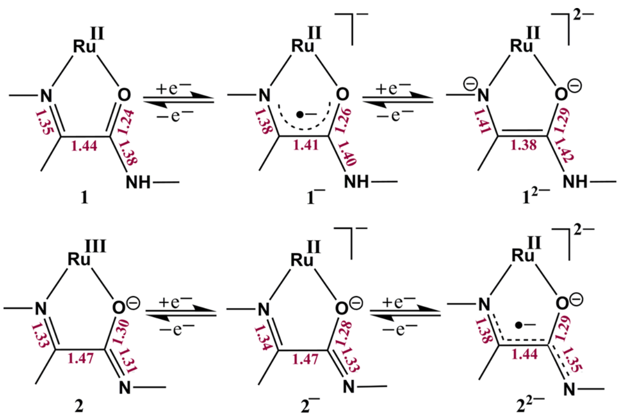

Scheme 6. Electronic Structural Forms of 1^n and 2^n

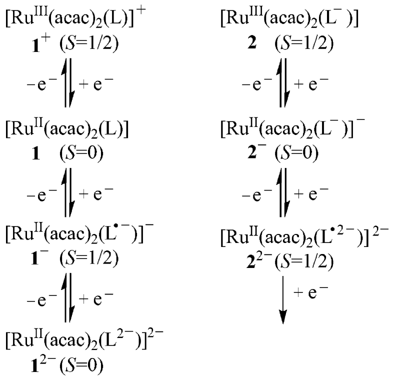

and Hallo in $[Ru^{II}(bpy)_2(DMA)](PF_6)_2$ (**3**) (Scheme 3) and $[Ru^{II}(Hallo)(tpa)]PF_6$ (**4**) (Scheme 3) occur at −0.23, −1.11 V and −0.94, −1.42 V versus SCE, respectively.[7,6a,19]

The one-electron paramagnetic Ru(III) state (S = 1/2) in isolated **2** or electrochemically generated $\mathbf{1}^+$ displays metal-based anisotropic axial EPR at 77 K in CH_3CN (Figure 7, Table 6) with $\langle g \rangle/\Delta g$ 2.136/0.488 or 2.084/0.364, respectively.[10,23] The reasonably higher $\langle g \rangle$ and Δg values of **2** as compared to $\mathbf{1}^+$ are attributed to more metal contribution in the singly occupied MO in **2**, as has also been reflected in the Mulliken spin distribution on the metal ions, 0.818 and 0.766, respectively (Table 5). Unfortunately, coulometrically generated paramagnetic $\mathbf{1}^-$ (Red1) and $\mathbf{2}^{2-}$ (Red2) (Figure 5) are found to be unstable under the experimental conditions, which indeed has prevented us from checking their EPR profiles.

The electronic structural forms of $\mathbf{1}^n$ (n = +1, 0, −1, −2) and $\mathbf{2}^n$ (n = 0, −1, −2) thus established via experimental and DFT calculations are highlighted in Scheme 6.

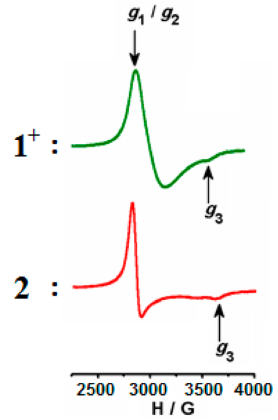

Figure 7. EPR spectra of 1^+ and **2** in CH_3CN at 77 K.

Table 6. EPR Data for 1^+ and 2 in CH_3CN at 77 K

	1^+	2
g_1	2.198	2.286
g_2	2.198	2.286
g_3	1.834	1.798
$\langle g\rangle^a$	2.084	2.136
Δg^b	0.364	0.488

[a] $\langle g\rangle = \{1/3(g_1^2 + g_2^2 + g_3^2)\}^{1/2}$. [b] $\Delta g = g_1 - g_3$.

Spectroelectrochemistry and TD-DFT Calculations. The origins of the experimental absorption spectra of complexes $\mathbf{1}^n$ (n = +1, 0, −1, −2) and $\mathbf{2}^n$ (n = 0, −1, −2) (Figure 8) have been interpreted via TD-DFT calculations (Table 7) based on the DFT-optimized structure in each redox state, which essentially reveal mixed metal–ligand and ligand-derived multiple transitions in the visible and UV region, respectively.[3b,6a,7] The complexes $(acac)_2Ru^{II}(L)$ (**1**) and $(acac)_2Ru^{III}(L^-)$ (**2**) exhibit distinct spectral features with one and two moderately intense visible region absorptions, λ_{max}/nm (ε/M^{-1} cm^{-1}) at 648 (7460) (TD-DFT: 600 nm) and 513 (4980) (TD-DFT: 534 nm), 411 (7530) (TD-DFT: 462 nm) corresponding to transitions of $(d\pi)Ru/(\pi)acac \rightarrow (\pi^*)L$ (MLLCT) and $(\pi)L^-/(\pi)acac \rightarrow (d\pi)Ru/(\pi^*)acac$ (LLMLCT), $(d\pi)Ru/(\pi)L^-/(\pi)acac \rightarrow (\pi^*)L^-$ (MLLLCT), respectively. On oxidation of **1** (Ru^{II} center) to 1^+ (Ru^{III} center) (Ox1 in Figure 5), the lowest energy band at 648 nm undergoes appreciable blue shifting to 543 nm (ε/M^{-1} cm^{-1}: 5820) (TD-DFT: 606 nm) with a reduction in intensity, which has been assigned by TD-DFT as $(\pi)acac/(d\pi)Ru/(\pi)L \rightarrow (d\pi)Ru/(\pi^*)acac$ based LMLMLCT transition. It also displays one $(\pi)acac/(d\pi)Ru \rightarrow (\pi^*)L$ LMLCT transition at 418 nm (ε/M^{-1} cm^{-1}: 5350) (TD-DFT: 480 nm). The first reduced complex, $[(acac)_2Ru^{II}(L^{\bullet -})]^-$ (1^-, Red1 in Figure 5), displays two $(d\pi)Ru/(\pi)acac \rightarrow (\pi^*)L$ (MLLCT) based intense visible transitions at 690 nm (ε/M^{-1} cm^{-1}: 11100) (TD-DFT: 730 nm) and 459 nm (ε/M^{-1} cm^{-1}: 7530) (TD-DFT: 391 nm). On further reduction to 1^{2-} (Red2, Figure 5), the visible region bands of 1^- are slightly shifted to 677 nm (ε/M^{-1} cm^{-1}: 2880) (TD-DFT: 613 nm) and 506 nm (ε/M^{-1} cm^{-1}: 8880) (TD-DFT: 506 nm), which correspond to $(\pi)L \rightarrow (\pi^*)L/(d\pi)Ru/(\pi^*)acac$ (LLMLCT) and $(d\pi)Ru/(\pi)acac \rightarrow (\pi^*)acac$ (MLLCT) transitions, respectively.

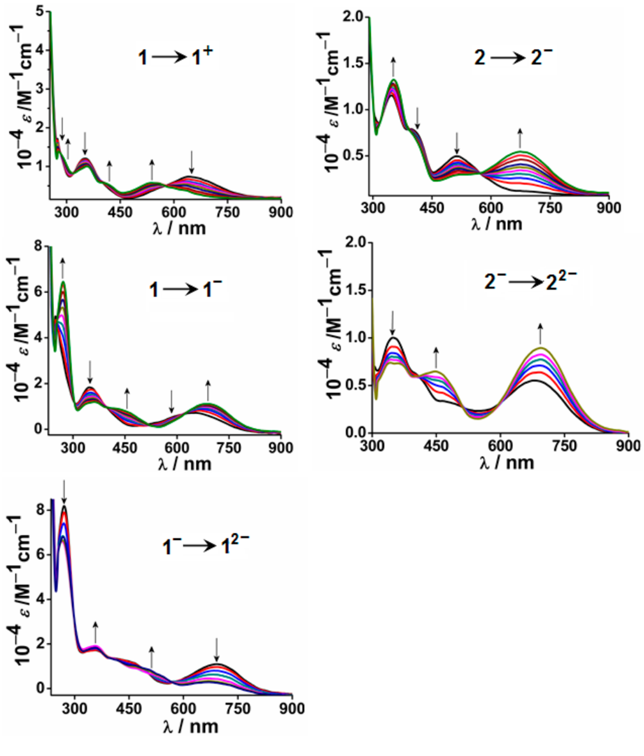

Figure 8. Electronic spectra of $\mathbf{1}^n$ and $\mathbf{2}^n$ in CH_3CN.

The lowest energy band of **2** (Ru^{III} center) at 513 nm (ε/M^{-1} cm^{-1}: 4980) (TD-DFT: 534 nm) is red-shifted to 678 nm (ε/M^{-1} cm^{-1}: 5560) (TD-DFT: 588 nm) with the enhancement of intensity on reduction to 2^- (Ru^{II} center) (Red1 in Figure 5), which is assigned to a $(d\pi)Ru/(\pi)acac \rightarrow (\pi^*)L^-$ based MLLCT transition. The second reduced state, 2^{2-} (Red2 in Figure 5), exhibits two visible bands at 695 nm (ε/M^{-1} cm^{-1}: 8990) (TD-DFT: 656 nm) and 451 nm (ε/M^{-1} cm^{-1}: 6470) (TD-DFT: 432 nm), which originate through $(d\pi)Ru/(\pi)L^- \rightarrow (\pi^*)acac/(\pi^*)L^-$ (MLLLCT) and $(d\pi)Ru/(\pi)acac \rightarrow (\pi^*)acac$ (MLLCT) transitions, respectively. $\mathbf{1}^n$ and $\mathbf{2}^n$ also display intense ligand (L, acac, or L^-)-based multiple interligand and intraligand transitions in the higher energy UV region.

Proton-Driven Processes. The pK_a values of complex **1** involving two NH protons associated with L are estimated by monitoring the change of its spectral profile (Figure 8, absorbance at 648 nm) with a gradual increase in pH (6–12)[24] in 1:1 CH_3CN–H_2O (Figure S4, Supporting Information), which gives pK_{a1} and pK_{a2} values of 6.5 and 8.16, respectively. Similarly, the pK_{a1} of **2** (Figure S4, Supporting Information) with one NH proton of L^- has been estimated (1:1 CH_3CN–H_2O) to be 8.43 by following its spectral profile in Figure 8 (absorbance at 513 nm) with the change in pH. The similarity of pK_{a2} of **1** (8.16) and pK_{a1} of **2** (8.43) essentially suggests that the deprotonation of the N3H proton of **1** (pK_{a1}, 6.5) occurs prior to the N1H proton (pK_a >8).

The addition of NaOH in **1** (1:1 molar ratio) or HCl in **2** (1:1 molar ratio) in CH_3CN leads to the formation of 2^- or 1^+, respectively (Figure 9). This has been authenticated via the identical spectral features of **1**+NaOH and electrochemically reduced 2^- as well as the same for **2**+HCl and electrochemically oxidized 1^+ (Figures 8, 9). This reveals the fact of base- and acid-driven simple abstraction and addition of protons at the more acidic N3 site in **1** and **2**, respectively, without any electron-transfer process.[25]

Table 7. TD-DFT (B3LYP/CPCM/CH_3CN)-Calculated Electronic Transitions for 1^n and 2^n

λ/nm expt (DFT)	ε/M^{-1} cm^{-1} (f)	transition	character
1 (S = 0)			
648 (600)	7460 (0.22)	HOMO−1 → LUMO(0.64)	Ru(dπ)/acac(π) → L(π*)
352 (328)	12220 (0.20)	HOMO−7 → LUMO(0.42)	L(π) → L(π*)
		HOMO−8 → LUMO(0.26)	acac(π)/L(π) → L(π*)
274 (238)	17260 (0.64)	HOMO−5 → LUMO+1(0.47)	L(π) → L(π*)
1^{+} (S = 1/2)			
543 (606)	5820 (0.05)	HOMO−2(β) → LUMO(β)(0.90)	acac(π)/Ru(dπ)/L(π) → Ru(dπ)/acac(π*)
418 (480)	5350 (0.04)	HOMO−1(α) → LUMO(α)(0.61)	acac(π)/Ru(dπ) → L(π*)
358 (348)	10000 (0.17)	HOMO−5(β) → LUMO+1(β)(0.63)	L(π) → L(π*)
277 (243)	13960 (0.18)	HOMO−13(β) → LUMO+1(β)(0.40)	L(π) → L(π*)
1^{-} (S = 1/2)			
690 (730)	11100 (0.10)	HOMO−1(β) → LUMO(β)(0.94)	Ru(dπ)/acac(π) → L(π*)
459 (391)	7530 (0.05)	HOMO−2(α) → LUMO(α)(0.55)	Ru(dπ)/acac(π) → acac(π*)
360 (311)	11940 (0.10)	HOMO(α) → LUMO+10(α)(0.63)	L(π)/Ru(dπ) → L(π*)/acac(π*)/Ru(dπ)
271 (237)	64550 (0.36)	HOMO−14(β) → LUMO(β)(0.45)	L(π)/acac(π) → L(π*)
		HOMO−6(α) → LUMO+2(α)(0.33)	acac(π)/L(π) → L(π*)
1^{2-} (S = 0)			
677 (613)	2880 (0.008)	HOMO → LUMO+2(0.70)	L(π) → L(π*)/Ru(dπ)/acac(π*)
506 (506)	8880 (0.005)	HOMO−1 → LUMO+1(0.61)	Ru(dπ)/acac(π) → acac(π*)
357 (355)	18580 (0.01)	HOMO → LUMO+8(0.64)	L(π)/acac(π) → acac(π*)/Ru(dπ)
267 (247)	66020 (0.12)	HOMO−7 → LUMO(0.36)	L(π)/acac(π) → acac(π*)
2 (S = 1/2)			
513 (534)	4980 (0.05)	HOMO−4(β) → LUMO(β)(0.74)	L^{-}(π)/acac(π) → Ru(dπ)/acac(π*)
411 (462)	7530 (0.06)	HOMO−1(α) → LUMO(α)(0.58)	Ru(dπ)/L^{-}(π)/acac(π) → L^{-}(π*)
347 (337)	11560 (0.14)	HOMO−5(α) → LUMO(α)(0.56)	acac(π)/L^{-}(π) → L^{-}(π*)
2^{-} (S = 0)			
678 (588)	5560 (0.22)	HOMO−1 → LUMO(0.65)	Ru(dπ)/acac(π) → L^{-}(π*)
404 (382)	7020 (0.08)	HOMO−4 → LUMO(0.58)	L^{-}(π)/acac(π) → L^{-}(π*)
		HOMO−5 → LUMO(0.26)	L^{-}(π)/acac(π) → L^{-}(π*)
352 (323)	13260 (0.09)	HOMO−6 → LUMO(0.48)	L^{-}(π) → L^{-}(π*)
2^{2-} (S = 1/2)			
695 (656)	8990 (0.04)	HOMO−1(β) → LUMO(β)(0.71)	Ru(dπ)/L^{-}(π) → acac(π*)/L^{-}(π*)
451 (432)	6470 (0.02)	HOMO−2(α) → LUMO(α)(0.66)	Ru(dπ)/acac(π) → acac(π*)
352 (360)	7340 (0.04)	HOMO−4(β) → LUMO(β)(0.35)	L^{-}(π)/acac(π) → acac(π*)/L^{-}(π*)
		HOMO(α) → LUMO+8(α)(0.36)	L^{-}(π) → acac(π*)/Ru(dπ)/L^{-}(π*)

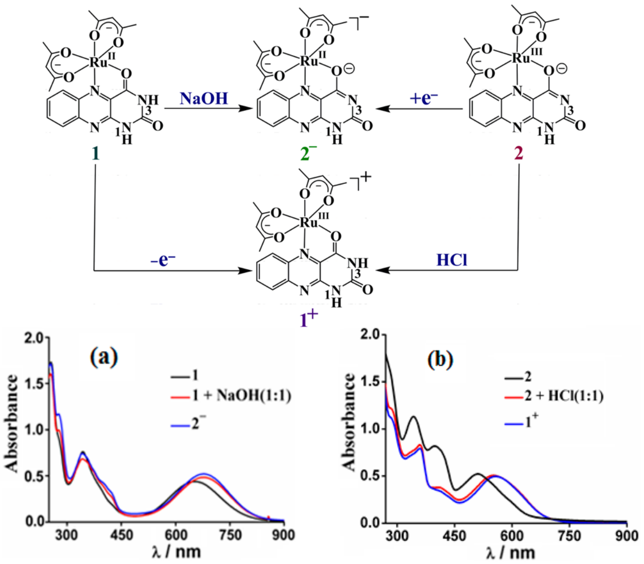

Figure 9. UV−vis spectra of (a) **1**, **1**+NaOH (1:1 molar ratio), and electrochemically reduced **2**$^{-}$ and (b) **2**, **2**+HCl (1:1 molar ratio), and electrochemically oxidized **1**$^{+}$ in CH_3CN.

■ CONCLUSION

In conclusion, the salient features of the present article including the outlook are highlighted below:

- The simple introduction of selective metal fragment {Ru(acac)$_2$} incorporating electron-rich acac^{-} facilitates the simultaneous stabilization of conventional α-iminoketo chelating and unprecedented α-iminoenolato chelating forms of alloxazine, a flavin analogue in {Ru^{II}(acac)$_2$}-derived **1** and {Ru^{III}(acac)$_2$}-derived **2**, respectively.
- The crystal structure of **2** reveals its hydrogen-bonded dimeric form as well as π−π interactions between the nearly planar tricyclic rings of alloxazine of nearby molecules.
- The electronic structural aspects of **1**^{n} (n = +1, 0, −1, −2) and **2**^{n} (n = 0, −1, −2) establish metal and alloxazine π-system based redox processes, (dπ)Ru^{II} → (π*)L back-bonding in **1**, and greater metal contribution in the singly occupied MO of **2** as compared to analogous **1**$^{+}$.
- The proton-driven internal reorganizations in **1** and **2** lead to the transformations of **1** (Ru^{II} state) → **2**$^{-}$ (Ru^{II} state) and **2** (Ru^{III} state) → **1**$^{+}$ (Ru^{III} state) without any electron-transfer process.

The revelation of a newer bonding motif of monodeprotonated alloxazine (L^-, α-iminoenolato chelating form) in **2** by the simple modulation of the electronic nature of the metal fragment may therefore be expected to extend further insights into the probable modes of metal–flavin interaction and its influence on the electron-transfer processes in biology.

■ EXPERIMENTAL SECTION

Materials. The metal precursor $Ru^{II}(acac)_2(CH_3CN)_2$ was prepared according to the literature-reported procedure.[26] Alloxazine (L) was purchased from Sigma-Aldrich. All other chemicals and reagents were of reagent grade and used without further purification. For spectroscopic and electrochemical studies HPLC-grade solvents were used.

Physical Measurements. The electrical conductivities of the complexes in CH_3CN were checked by using a Systronic 305 conductivity bridge. ^1H NMR spectra were recorded using a Bruker Avance III 500 MHz. FT-IR spectra were recorded on a Nicolet spectrophotometer with samples prepared as KBr pellets. Cyclic voltammetry measurements were performed on a PAR model 273A electrochemistry system. A glassy carbon working electrode, a platinum wire auxiliary electrode, and a saturated calomel reference electrode (SCE) were used in a standard three-electrode configuration cell. A platinum wire-gauze working electrode was used for the constant-potential coulometry experiment. UV–vis spectroelectrochemical studies were performed on a BAS SEC2000 spectrometer system. The supporting electrolyte was Et_4NClO_4, and the solute concentration was $\sim 10^{-3}$ M. All electrochemical experiments were carried out under a dinitrogen atmosphere at 298 K. The half-wave potential E^0 was set equal to 0.5 ($E_{pa} + E_{pc}$), where E_{pa} and E_{pc} are anodic and cathodic cyclic voltammetry peak potentials, respectively. The elemental analyses were carried out on a Thermoquest (EA 1112) microanalyzer. Electrospray mass spectra (ESI-MS) were recorded on a Bruker Maxis Impact (282001.00081).

Crystallography. Single crystals of **2** were grown by slow evaporation of its 2:1 dichloromethane–methanol solution mixture. X-ray crystal data were collected on a Rigaku SATURN-724+ CCD single crystal X-ray diffractometer. Data collection was evaluated by using the CrystalClear-SM Expert software. The data were collected by the standard ω-scan technique. The structure was solved by the direct method using SHELXS-97 and refined by full matrix least-squares with SHELXL-97, refining on F^2.[27] All non-hydrogen atoms were refined anisotropically. The hydrogen atoms were placed in geometrically constrained positions (except N1H) and refined with isotropic temperature factors, generally $1.2U_{eq}$ of their parent atoms. Hydrogen atoms were included in the refinement process as per the riding model.

Computational Details. Full geometry optimizations were carried out by using the density functional theory method at the (R)B3LYP level for **1**, $\mathbf{1}^{2-}$, and $\mathbf{2}^-$ and the (U)B3LYP level for $\mathbf{1}^+$, $\mathbf{1}^-$, **2**, and $\mathbf{2}^{2-}$.[28] Except ruthenium all other elements were assigned the 6-31G* basis set. The LANL2DZ basis set with effective core potential was employed for the ruthenium atom.[29] The vibrational frequency calculations were performed to ensure that the optimized geometries represent the local minima and there are only positive eigenvalues. All calculations were performed with the Gaussian09 program package.[30] Vertical electronic excitations based on (R)B3LYP/(U)B3LYP-optimized geometries were computed for $\mathbf{1}^n$ (n = +1, 0, −1, −2) and $\mathbf{2}^n$ (n = 0, −1, −2) using the time-dependent density functional theory (TD-DFT) formalism[31] in acetonitrile using the conductor-like polarizable continuum model (CPCM).[32] Chemissian 1.7[33] was used to calculate the fractional contributions of various groups to each molecular orbital. All calculated structures were visualized with ChemCraft.[34]

Synthesis of $[(acac)_2Ru^{II}(L)]$, 1, and $[(acac)_2Ru^{III}(L^-)]$, 2. The precursor complex $[Ru^{II}(acac)_2(CH_3CN)_2]$ (100 mg, 0.260 mmol) and the ligand, alloxazine (L) (56 mg, 0.260 mmol), were taken in 50 mL of methanol, and the mixture was heated to reflux for 8 h under aerobic conditions. The initial orange solution gradually changed to bluish-green. The reaction mixture was evaporated to dryness under reduced pressure and purified by column chromatography on a silica gel (mesh 60–120) column. The bluish-green complex **1** was initially eluted by a solvent mixture of CH_2Cl_2–CH_3CN (1:1) followed by reddish complex **2** by a CH_3CN–MeOH (30:1) solvent mixture. Evaporation of solvent under reduced pressure yielded the pure complexes **1** and **2**.

1: Yield: 54% (72 mg). ^1H NMR (500 MHz) in CD_3CN [δ/ppm (J/Hz)]: 9.60 (b, 2H, (NH, L)), 8.03 (d, 9.50, 1H, L), 7.84 (t, 8.20, 8.10, 1H, L), 7.76 (d, 7.50, 1H, L), 7.52 (t, 8.80, 8.65, 1H, L), 5.68 (s, 1H, CH(acac)), 5.25 (s, 1H, CH(acac)), 2.32 (s, 3H, CH_3(acac)), 2.03 (s, 3H, CH_3(acac)), 2.01 (s, 3H, CH_3(acac)), 1.95 (s, 3H, CH_3(acac)). MS (ESI+, CH_3CN): m/z {**1**} calcd 514.0420; found 514.0449. IR (KBr): ν(C=O, cm^{-1}): 1713. Molar conductivity (CH_3CN): $\Lambda_M = 6\ \Omega^{-1}\ cm^2\ M^{-1}$. Anal. Calcd (%) for $C_{20}H_{20}N_4O_6Ru$: C, 46.78; H, 3.93; N, 10.91. Found: C, 46.55; H, 3.98; N, 10.99.

2: Yield: 26% (35 mg). ^1H NMR (500 MHz) in $CDCl_3$ [δ/ppm (J/Hz)]: 6.57 (b, 1H, L^-), 6.22 (b, 1H, L^-), 5.40 (b, 2H, L^-), 4.95 (b, 1H (NH, L^-)), −14.38 (b, 2H, CH(acac)), −19.82 (b, 12H, CH_3(acac)). MS (ESI+, CH_3CN): m/z {**2**} calcd 513.0348; found 513.2674. IR (KBr): ν(C=O, cm^{-1}): 1667. Molar conductivity (CH_3CN): $\Lambda_M = 4\ \Omega^{-1}\ cm^2\ M^{-1}$. Anal. Calcd (%) for $C_{20}H_{19}N_4O_6Ru$: C, 46.87; H, 3.74; N, 10.93. Found: C, 46.75; H, 3.86; N, 10.87.

■ ASSOCIATED CONTENT

Ⓢ Supporting Information

X-ray crystallographic file in CIF format for **2**, mass spectra (Figure S1), DFT-optimized structures for **1** and **2** (Figures S2, S3), plot of absorbance versus pH for **1** and **2** (Figure S4), bond parameters for $\mathbf{1}^n$ and $\mathbf{2}^n$ (Tables S1–S4), MO compositions for $\mathbf{1}^n$ and $\mathbf{2}^n$ (Tables S5–S11). This material is available free of charge via the Internet at http://pubs.acs.org. CCDC 1043694 (**2**) contain supplementary crystallographic data for this paper. These data can be obtained free of charge from the Cambridge Crystallographic Data Center via www.ccdc.cam.ac.uk/data_request/cis.

■ AUTHOR INFORMATION

Corresponding Author

*E-mail: lahiri@chem.iitb.ac.in (G. K. Lahiri).

Notes

The authors declare no competing financial interest.

■ ACKNOWLEDGMENTS

Financial support received from the Department of Science and Technology, Council of Scientific and Industrial Research (fellowship to P.M. and A.D.), and University Grants Commission (fellowship to R.R.), New Delhi (India), is gratefully acknowledged.

■ DEDICATION

Dedicated to Professor Animesh Chakravorty on the occasion of his 80th birthday.

■ REFERENCES

(1) (a) Fraaije, M. W.; Mattevi, A. *Trends Biochem. Sci.* **2000**, *25*, 126–132. (b) Walsh, C. T. *Acc. Chem. Res.* **1980**, *13*, 148–155. (c) Walsh, C. T. *Acc. Chem. Res.* **1986**, *19*, 216–221. (d) Clarke, M. J. *Comments Inorg. Chem.* **1984**, *3*, 133–151. (e) Clarke, M. J. *Rev. Inorg. Chem.* **1980**, *2*, 27–52. (f) Bruice, T. C. *Acc. Chem. Res.* **1980**, *13*, 256–262.

(2) (a) *Flavins and Flavoproteins*; Yagi, K., Ed.; de Gruyter: Berlin, 1994. (b) *Chemistry and Biochemistry of the Flavoenzymes*; Muller, F., Ed.; CRC Press: Boca Raton, FL, 1991. (c) Hagen, W. R.; Arendsen, A. F. *Struct. Bonding Berlin* **1998**, *90*, 161–192. (d) Hemmerich, P.; Veeger, C.; Wood, H. C. S. *Angew. Chem., Int. Ed. Engl.* **1965**, *4*, 671–

687. (e) *Inorganic Chemistry*; Hemmerich, P.; Lauterwein, J.; Eichhorn, G. I., Eds.; Elsevier: Amsterdam, 1973; pp 1168−1189. (f) Lauterwein, J.; Hemmerich, P.; Lhoste, J. M. *Inorg. Chem.* **1975**, *14*, 2152−2161. (g) Wade, T. D.; Fritchie, C. J., Jr. *J. Biol. Chem.* **1973**, *248*, 2337−2343. (h) Fritchie, C. J., Jr. *J. Biol. Chem.* **1973**, *248*, 7516−7521. (i) Clarke, M. J.; Dowling, M. G.; Garafalo, A. R.; Brennan, T. F. *J. Am. Chem. Soc.* **1979**, *101*, 223−225.

(3) (a) Beinert, H.; Massey, V. *Trends Biol. Sci.* **1982**, *7*, 43−44. (b) Kaim, W.; Schwederski, B.; Heilmann, O.; Hornung, F. M. *Coord. Chem. Rev.* **1999**, *182*, 323−342.

(4) (a) Clarke, M. J.; Dowling, M. G.; Garafalo, A. R.; Brennan, T. F. *J. Biol. Chem.* **1980**, *255*, 3472−3481. (b) Dowling, M. G.; Clarke, M. J. *Inorg. Chim. Acta* **1983**, *78*, 153−160. (c) Clarke, M. J.; Dowling, M. G. *Inorg. Chem.* **1981**, *20*, 3506−3514.

(5) (a) Fritchie, C. J., Jr. *J. Chem. Soc., Chem. Commun.* **1972**, 1220−1221. (b) Benno, R. H.; Fritchie, C. J., Jr. *Acta Crystallogr. B* **1973**, *29*, 2493−2502. (c) Yu, M. W.; Fritchie, C. J., Jr. *J. Biol. Chem.* **1975**, *250*, 946−951. (d) Fritchie, C. J., Jr. *J. Biol. Chem.* **1972**, *247*, 7459−7464. (e) Garland, W. T., Jr.; Fritchie, C. J., Jr. *J. Biol. Chem.* **1974**, *249*, 2228−2234. (f) Heilmann, O.; Hornung, F. M.; Fiedler, J.; Kaim, W. *J. Organomet. Chem.* **1999**, *589*, 2−10.

(6) (a) Miyazaki, S.; Ohkubo, K.; Kojima, T.; Fukuzumi, S. *Angew. Chem., Int. Ed.* **2007**, *46*, 905−908. (b) Miyazaki, S.; Kojima, T.; Fukuzumi, S. *J. Am. Chem. Soc.* **2008**, *130*, 1556−1557.

(7) Hornung, F. M.; Heilmann, O.; Kaim, W.; Zális, S.; Fiedler, J. *Inorg. Chem.* **2000**, *39*, 4052−4058.

(8) Inui, Y.; Shiro, M.; Kusukawa, T.; Fukuzumi, S.; Kojima, T. *Dalton Trans.* **2013**, *42*, 2773−2778.

(9) (a) Das, D.; Sarkar, B.; Kumbhakar, D.; Mondal, T. K.; Mobin, S. M.; Fiedler, J.; Urbanos, F. A.; Jiménez-Aparicio, R.; Kaim, W.; Lahiri, G. K. *Chem.—Eur. J.* **2011**, *17*, 11030−11040. (b) Das, D.; Agarwala, H.; Chowdhury, A. D.; Patra, T.; Mobin, S. M.; Sarkar, B.; Kaim, W.; Lahiri, G. K. *Chem.—Eur. J.* **2013**, *19*, 7384−7394. (c) Das, D.; Das, A. K.; Sarkar, B.; Mondal, T. K.; Mobin, S. M.; Fiedler, J.; Zális, S.; Urbanos, F. A.; Jiménez-Aparicio, R.; Kaim, W.; Lahiri, G. K. *Inorg. Chem.* **2009**, *48*, 11853−11864. (d) Das, A.; Kundu, T.; Mobin, S. M.; Priego, J. L.; Jiménez-Aparicio, R.; Lahiri, G. K. *Dalton Trans.* **2013**, *42*, 13733−13746.

(10) Ghosh, P.; Mondal, P.; Ray, R.; Das, A.; Bag, S.; Mobin, S. M.; Lahiri, G. K. *Inorg. Chem.* **2014**, *53*, 6094−6106.

(11) Miyazaki, S.; Kojima, T.; Sakamoto, T.; Matsumoto, T.; Ohkubo, K.; Fukuzumi, S. *Inorg. Chem.* **2008**, *47*, 333−343.

(12) Kaufmann, H. L.; Carroll, P. J.; Burgmayer, S. J. N. *Inorg. Chem.* **1999**, *38*, 2600−2606.

(13) Kojima, T.; Inui, Y.; Miyazaki, S.; Shiroc, M.; Fukuzumi, S. *Chem. Commun.* **2009**, 6643−6645.

(14) (a) Matsuzawa, H.; Ohashi, Y.; Kaizu, Y.; Kobayashi, H. *Inorg. Chem.* **1988**, *27*, 2981−2885. (b) Kar, S.; Chanda, N.; Mobin, S. M.; Urbanos, F. A.; Niemeyer, M.; Puranik, V. G.; Jiménez-Aparicio, R.; Lahiri, G. K. *Inorg. Chem.* **2005**, *44*, 1571−1579. (c) Das, A.; Scherer, T. M.; Mobin, S. M.; Kaim, W.; Lahiri, G. K. *Inorg. Chem.* **2012**, *51*, 4390−4397. (d) Kumbhakar, D.; Sarkar, B.; Maji, S.; Mobin, S. M.; Fiedler, J.; Urbanos, F. A.; Jiménez-Aparicio, R.; Kaim, W.; Lahiri, G. K. *J. Am. Chem. Soc.* **2008**, *130*, 17575−17583. (e) Maji, S.; Sarkar, B.; Mobin, S. M.; Fiedler, J.; Urbanos, F. A.; Jimenez-Aparicio, R.; Kaim, W.; Lahiri, G. K. *Inorg. Chem.* **2008**, *47*, 5204−5211. (f) Ghumaan, S.; Sarkar, B.; Maji, S.; Puranik, V. G.; Fiedler, J.; Urbanos, F. A.; Jiménez-Aparicio, R.; Kaim, W.; Lahiri, G. K. *Chem.–Eur. J.* **2008**, *14*, 10816−10828.

(15) (a) Kumbhakar, D.; Sarkar, B.; Das, A.; Das, A. K.; Mobin, S. M.; Fiedler, J.; Kaim, W.; Lahiri, G. K. *Dalton Trans.* **2009**, 9645−9652. (b) Odani, A.; Masuda, H.; Inukai, K.; Yamauchi, O. *J. Am. Chem. Soc.* **1992**, *114*, 6294−6300.

(16) (a) Mitsumi, M.; Toyoda, J.; Nakasuji, K. *Inorg. Chem.* **1995**, *34*, 3367−3370. (b) Hunter, C. A.; Sanders, J. K. M. *J. Am. Chem. Soc.* **1990**, *112*, 5525−5534.

(17) Günther, A.; Nieto, P.; Berden, G.; Oomensbc, J.; Dopfer, O. *Phys. Chem. Chem. Phys.* **2014**, *16*, 14161−14171.

(18) (a) Koiwa, T.; Masuda, Y.; Shono, J.; Kawamoto, Y.; Hoshino, Y.; Hashi-moto, T.; Natarajan, K.; Shimizu, K. *Inorg. Chem.* **2004**, *43*, 6215−6223. (b) Das, A.; Scherer, T. M.; Mondal, P.; Mobin, S. M.; Kaim, W.; Lahiri, G. K. *Chem.—Eur. J.* **2012**, *18*, 14434−14443. (c) Mandal, A.; Agarwala, H.; Ray, R.; Plebst, S.; Mobin, S. M.; Priego, J. L.; Jiménez-Aparicio, R.; Kaim, W.; Lahiri, G. K. *Inorg. Chem.* **2014**, *53*, 6082−6093.

(19) Connelly, N. G.; Geiger, W. E. *Chem. Rev.* **1996**, *96*, 877−910.

(20) (a) Eriksson, L. E. G.; Ethrenberg, A. *Acta Chem. Scand.* **1964**, *18*, 1437−1453. (b) Heilmann, O.; Hornung, F. M.; Kaim, W.; Fiedler, J. *J. Chem. Soc., Faraday Trans.* **1996**, *92*, 4233−4238.

(21) (a) Kalinina, D.; Dares, C.; Kaluarachchi, H.; Potvin, P. G.; Lever, A. B. P. *Inorg. Chem.* **2008**, *47*, 10110−10126. (b) da Cunha, C. J.; Dodsworth, E. S.; Monteiro, M. A.; Lever, A. B. P. *Inorg. Chem.* **1999**, *38*, 5399−5409. (c) Masui, H.; Lever, A. B. P.; Dodsworth, E. S. *Inorg. Chem.* **1993**, *32*, 258−267.

(22) (a) Patra, S.; Sarkar, B.; Maji, S.; Fiedler, J.; Urbanos, F. A.; Jiménez-Aparicio, R.; Kaim, W.; Lahiri, G. K. *Chem.—Eur. J.* **2006**, *12*, 489−498. (b) Kar, S.; Sarkar, B.; Ghumaan, S.; Janardanan, D.; van Slageren, J.; Fiedler, J.; Puranik, V. G.; Sunoj, R. B.; Kaim, W.; Lahiri, G. K. *Chem.—Eur. J.* **2005**, *11*, 4901−4911.

(23) (a) Patra, S.; Sarkar, B.; Mobin, S. M.; Kaim, W.; Lahiri, G. K. *Inorg. Chem.* **2003**, *42*, 6469−6473. (b) Kundu, T.; Mobin, S. M.; Lahiri, G. K. *Dalton Trans.* **2010**, *39*, 4232−4242. (c) Mandal, A.; Kundu, T.; Ehret, F.; Bubrin, M.; Mobin, S. M.; Kaim, W.; Lahiri, G. K. *Dalton Trans.* **2014**, *43*, 2473−2487.

(24) (a) Cui, Y.; Mo, H.-J.; Chen, C.-J.; Niu, Y.-L.; Zhong, Y.-R.; Zheng, K.-C.; Ye, B.-H. *Inorg. Chem.* **2007**, *46*, 6427−6436. (b) Mo, H.-J.; Niu, Y.-L.; Zhang, M.; Qiao, Z.-P.; Ye, B.-H. *Dalton Trans.* **2011**, *40*, 8218−8225. (c) Das, A.; Agarwala, H.; Kundu, T.; Ghosh, P.; Mondal, S.; Mobin, S. M.; Lahiri, G. K. *Dalton Trans.* **2014**, *43*, 13932−13947.

(25) Ghosh, P.; Ray, R.; Das, A.; Lahiri, G. K. *Inorg. Chem.* **2014**, *53*, 10695−10707.

(26) Kobayashi, T.; Nishina, Y.; Shimizu, K. G.; Satô, G. P. *Chem. Lett.* **1988**, 1137−1140.

(27) (a) Sheldrick, G. M. *Acta Crystallogr., Sect. A* **2008**, *A64*, 112−122. (b) *Program for Crystal Structure Solution and Refinement*; University of Goettingen: Goettingen, Germany, 1997.

(28) Lee, C.; Yang, W.; Parr, R. G. *Phys. Rev. B* **1988**, *37*, 785−789.

(29) (a) Andrae, D.; Haeussermann, U.; Dolg, M.; Stoll, H.; Preuss, H. *Theor. Chim. Acta* **1990**, *77*, 123−141. (b) Fuentealba, P.; Preuss, H.; Stoll, H.; Szentpaly, L. V. *Chem. Phys. Lett.* **1989**, *89*, 418−422.

(30) Frisch, M. J.; Trucks, G. W.; Schlegel, H. B.; Scuseria, G. E.; Robb, M. A.; Cheeseman, J. R.; Scalmani, G.; Barone, V.; Mennucci, B.; Petersson, G. A.; Nakatsuji, H.; Caricato, M.; Li, X.; Hratchian, H. P.; Izmaylov, A. F.; Bloino, J.; Zheng, G.; Sonnenberg, J. L.; Hada, M.; Ehara, M.; Toyota, K.; Fukuda, R.; Hasegawa, J.; Ishida, M.; Nakajima, T.; Honda, Y.; Kitao, O.; Nakai, H.; Vreven, T.; Montgomery, J. A.; Peralta, Jr. J. E.; Ogliaro, F.; Bearpark, M.; Heyd, J. J.; Brothers, E.; Kudin, K. N.; Staroverov, V. N.; Kobayashi, R.; Normand, J.; Raghavachari, K.; Rendell, A.; Burant, J. C.; Iyengar, S. S.; Tomasi, J.; Cossi, M.; Rega, N.; Millam, J. M.; Klene, M.; Knox, J. E.; Cross, J. B.; Bakken, V.; Adamo, C.; Jaramillo, J.; Gomperts, R.; Stratmann, R. E.; Yazyev, O.; Austin, A. J.; Cammi, R.; Pomelli, C.; Ochterski, J. W.; Martin, R. L.; Morokuma, K.; Zakrzewski, V. G.; Voth, G. A.; Salvador, P.; Dannenberg, J. J.; Dapprich, S.; Daniels, A. D.; Farkas, O.; Foresman, J. B.; Ortiz, J. V.; Cioslowski, J.; Fox, D. J. *Gaussian 09* (Revision A.02); Gaussian, Inc.: Wallingford, CT, 2009.

(31) (a) Bauernschmitt, R.; Ahlrichs, R. *Chem. Phys. Lett.* **1996**, *256*, 454−464. (b) Stratmann, R. E.; Scuseria, G. E.; Frisch, M. J. *J. Chem. Phys.* **1998**, *109*, 8218−8225. (c) Casida, M. E.; Jamorski, C.; Casida, K. C.; Salahub, D. R. *J. Chem. Phys.* **1998**, *108*, 4439−4450.

(32) (a) Barone, V.; Cossi, M. *J. Phys. Chem. A* **1998**, *102*, 1995−2001. (b) Cossi, M.; Barone, V. *J. Chem. Phys.* **2001**, *115*, 4708−4718. (c) Cossi, M.; Rega, N.; Scalmani, G.; Barone, V. *J. Comput. Chem.* **2003**, *24*, 669−681.

(33) O'Boyle, N. M.; Tenderholt, A. L.; Langner, K. M. *J. Comput. Chem.* **2008**, *29*, 839−845.

(34) Zhurko, D. A.; Zhurko, G. A. *ChemCraft 1.5*; Plimus: San Diego, CA. Available at http://www.chemcraftprog.com.